Rare earth oxide doping and synthesis of spinel ZnMn$_2$O$_4$/KIT-1 with double gyroidal mesopores for desulfurization nature of hot coal gas

Qiang Liu[1], Zhaofei Zhang[1], Bingsi Liu[*], Hong Xia

Department of Chemistry, Tianjin University, and the National Collaborative Innovation Center of Chemical Science and Engineering (Tianjin), Tianjin 300072, People's Republic of China

ABSTRACT

In this work, spinel ZnMn$_2$O$_4$/KIT-1 using KIT-1 with 3-dimensional wormhole-like channels as support was fabricated for hot coal gas desulfurization at high temperature *via* a sol-gel method. Effects of ZnMn$_2$O$_4$ contents, desulfurization temperature, rare earth oxide doping and steam volume on the desulfurization performances of ZnMn$_2$O$_4$/KIT-1 were investigated systematically. A superior sorbent of ZnMn(Ce)$_2$O$_4$/KIT-1 was obtained with the addition of 45%ZnMn$_2$O$_4$ and doping of CeO$_2$, which was suitable for 550 °C desulfurization and endured a small impact of steam. Moreover, the crystal lattice replace between Ce^{3+} and Mn^{3+} facilitated the dispersion of active species and avoided Zn^{2+} converting to elemental Zn. The high sulfur capacity of ZnMn(Ce)$_2$O$_4$/KIT-1 was maintained after five consecutive desulfurization-regeneration cycles. The textural properties of sorbents were evaluated successively by means of XRD, BET, HRTEM, XPS, H$_2$-TPR and TG/DSC techniques. Results revealed that the main active components in sorbent were robustly existed in form of ZnMn$_2$O$_4$ spinel which effectually prevented the vaporization of Zn in high temperature. Therefore, a low-cost sorbent of ZnMn(Ce)$_2$O$_4$/KIT-1 with the high *BSC* (171.7 mg S/g sorbent) has an excellent performance for H$_2$S removal from hot coal gas.

1. Introduction

Environmental pollution and energy shortage are serious problems which restrict the industrial production and economic development [1]. Although new energy sources are applied in our lives, coal is still regarded as an important power plant source currently due to its huge advantages of abundance, stability and low cost [2]. However, coal-fired power plants using conventional operation systems easily caused many problems in respect of atmospheric pollution, such as primary fine particulate matter (PM$_{2.5}$) [3]. Besides, hydrogen sulfide (H$_2$S) hided in the fossil fuel is the main culprit that destroys downstream equipments and the direct discharge of untreated flue gas with sulfur dioxide (SO$_2$) will cause the acid rain [4,5]. Based on the efficient reduction of pollution emission and improvement of fuel utilization, the clean coal technologies (CCT) are widely accepted and used to purify unburned fuels in recent decades [6,7]. The development of thermal power station equipped with the integrated coal gasification combined cycle (IGCC) is the promising approach for the conversion of coal resource into high-octane fuel [8]. The hot gas desulfurization (HGD) is a crucial strategy before the combustion of coal gas in the IGCC system due to its high rate in thermal energy utilization [9]. Until now, a variety of green desulphurizers have been explored and developed to directly remove the toxic gas of H$_2$S for the production of ultra clean fuels [10]. The desulfurization temperature of 350–600 °C will apt to methanol and Fischer-Tropsch synthesis procedure whereas the desulfurization temperature for IGCC system is more than 700 °C [11]. Transition metal oxides and rare earth oxides are thus suitable candidates mostly used as active components in desulphurizers for their high efficacy with low cost, such as zinc oxide (ZnO), ferric oxide, cupric oxide, manganese oxide (MnO), cerium oxide *etc*, or the mixture of oxides mentioned above [12,13].

Among all these sorbents, ZnO owns the most favorable thermodynamics to keep the stabilities of active species on removal of H$_2$S at high temperature [14]. Especially the generated ZnS in desulfurization process, which can be converted to ZnO easily under the regeneration treatment of steam or air [15]. The utilization of ZnO sorbent, however, is limited in two ways: by the slow gas-film diffusion on sulfidation kinetics, and by the inner ZnO species covered with the formation of dense ZnS layer which is hard to contact with H$_2$S [16]. Furthermore, the vaporization of Zn during the reduction process in high reducing atmosphere of hot coal is also a significant problem [17]. Adding other enhanced components to the activating oxide as structure stabilizers

---

will overcome these defects. Another metal oxide, MnO, is a familiar active component with high sulfur capacity, which has the highest initial reaction rate with H_2S under the condition of 400–800 °C [18]. Moreover, MnS is readily converted to MnO in reduction atmosphere, but cannot be further reduced to elemental Mn below 1200 °C [19]. Nevertheless, the shortcoming that decreased slightly desulfurization efficiency at higher temperature is also existed in use of MnO sorbent [20]. Recent studies have noted that sorbents of multi-component produced by various metal oxides could make up for the shortcoming of each component and ameliorate sorbent property [21]. So Mn-based sorbents have great potential that present the excellent desulfurization reactivity and high sulfur capacity after adding other elements, such as the aforementioned Zn and Ce [22].

Notably, spinel phase oxides with the general formula of AB_2O_4 (A, B = metal) have attracted considerable attention because of their stable structures and diverse functions [23,24]. With the repeating cubical $[Mn_4O_4]^{4+}$ cores, $ZnMn_2O_4$ sorbent which incorporates two different metal atoms has greater activity than the layered polymorphs possessing incomplete cube Mn_3O_4 repeating units [25]. Ko et al. [26] have successfully prepared a series of $ZnMn_2O_4$ spinel sorbents supported by SiO_2, ZrO_2 and γ-Al_2O_3, respectively. With the formation of $ZnMn_2O_4$ spinel, no significant vaporization of Zn was observed when these sorbents were employed at 600 °C. However the utilization of sorbent decreased when the content of Zn-Mn oxides reached to 30 *wt.*%, which was ascribed to the low surface area of used supports. But only a few researchers focus on the development of spinel structures of ternary transition metal oxides and investigation of their site-preferences [27].

Except for active species needed in sorbents, supports also play a vital role in sulfidation reaction. They can make active metal oxides fully dispersing on themselves to increase the exposed functional surface and provide an adequate place for the speedy transport of reactions [28]. Mesoporous silica with high surface area, large pore volume and narrow pore distribution, such as MCM-41, SBA-15 and HMS, has already been used as support to prepare desulphurizer [22,29]. Aside from the above supports, KIT-1 with the special structure of 3-dimensional wormhole-like channels can be more resistant to pore blocking [30]. Double gyroidal mesopores of KIT-1 will allow the rapid transport of H_2S gas and improve further its diffusion on the active adsorption sites [31]. In this work, KIT-1 with high specific surface area was selected as the support to load $ZnMn_2O_4$ spinel phase. In order to further enhance desulfurization performance, three rare earth oxides (La_2O_3, CeO_2 and Sm_2O_3) were successfully involved in this study to modify the sorbent. The desulfurization behaviors of a series of $ZnMn_2O_4$/KIT-1 sorbents with different contents were detected at a fixed bed reactor under different conditions systematically. Effect of steam content as well as the regenerate ability of sorbent was explored as follows.

2. Experimental methods

2.1. Synthesis of support

KIT-1 was synthesized according to the report in literature [31]. At first, 12.8 g of cetyltrimethylammonium chloride (CTAC) and 45.62 g of ethylenediaminetetraacetic acid sodium (EDTANa$_4$) were dissolved into 300 mL of deionized water (DW). Afterwards, 16.37 g of water glass was added to the aforementioned solution and stirred until the uniform sol was formed. The obtained sol was transferred into a sealed Teflon-lined autoclave for hydrothermal synthesis of 48 h at 100 °C. Finally, the mixture was filtered, washed and dried, and calcined at 550 °C for 6 h to obtain KIT-1.

2.2. Preparation of sorbents

Different loading percentages of $ZnMn_2O_4$ with same molar ratio (Zn/Mn = 1/2) onto mesoporous KIT-1 were synthesized by a sol-gel method. For example, 45%$ZnMn_2O_4$/KIT-1 was prepared as follows:

5.38 g of $Mn(NO_3)_2$ solution (50 *wt.*%) and 2.24 g of $Zn(NO_3)_2$·$6H_2O$ was added to 25 mL of DW. After the addition of citric acid with a molar amount of 1.5 times of metal ions, 2.2 g of as-prepared KIT-1 was mixed in the aforementioned solution. The mixture was kept at 60 °C with stirring continuously until a viscous gel generated. Subsequently, the gel was aged at ambient temperature for 72 h. The sample was calcined at 600 °C for 6 h in the end. The obtained $ZnMn_2O_4$/KIT-1 sorbents were denoted as x%$ZnMn_2O_4$/KIT-1 (x = 25, 35, 45, 55), respectively according to their metal oxides contents. Besides, 45%$ZnMn_2O_4$/ KIT-1 sorbents with different addition of rare earth oxides (5 *wt.*%) were prepared under same condition, and denoted as $ZnMn(La)_2O_4$/KIT-1, $ZnMn(Ce)_2O_4$/KIT-1 and $ZnMn(Sm)_2O_4$/KIT-1, respectively, which indicated that rare earth element occupied the sites of Mn by crystal lattice replace in $ZnMn_2O_4$ spinel. All characterization methods were given in Supplementary materials.

2.3. Desulfurization/regeneration assessments

Desulfurization tests were performed at atmospheric pressure in a fixed-bed quartz microreactor (*i.d.* 10 mm, loaded 0.5 g of sorbent) using simulated hot coal gas within or without steam (0.33% H_2S, 10.6% H_2, 28% CO and N_2 as balance). The flow rates of feed gas were controlled by a mass flow-meter (D07-7B/ZM, Beijing Sevenstar Electronics Co., Ltd., China). A thermocouple placed in the center of the sorbent bed was used to control the reaction temperature. The sorbent bed was heated to the reaction temperature with the rate of 10 °C min^{-1} in N_2 atmosphere. After desulfurization process, the pure N_2 was used to purge the system until the sorbent bed was cooled to ambient temperature. The concentration of H_2S in the inlet/outlet gas was analyzed by the method of iodometric titration with absolute deviation of 50 mg m^{-3}. The effects of $ZnMn_2O_4$ content (25–55 *wt.*%), desulfurization temperature (500–650 °C), rare earth oxide doping (La_2O_3, CeO_2 and Sm_2O_3) and steam volume (0–20 *vol.*%) on H_2S removal from coal gas by sorbents were explored in turn. The breakthrough point, defined as the breakthrough sulfur capacity (*BSC*, mg S/g sorbent), was determined when the concentration of H_2S below 50 mg m^{-3} in the outlet. Herein, the sulfur capacity (*SC*) and sorbent utilization (*SU*) were calculated by the formula, respectively [32]:

$$SC\left(\frac{mg sulfur}{g\, sorbent}\right) = GHSV \times \frac{M_s}{V_m} \times \frac{22.4}{M_{H_2S}} \times \left[\int_0^t (C_{in} - C_{out})dt\right] \times 10^{-3}$$

(1)

$$SU = BSC/TSC \times 100\%$$

(2)

Where, *GHSV* (L h^{-1} g^{-1}) is the weight hourly space velocity; *M*s and M_{H2S} are the molar weight of S (32.06 g mol^{-1}) and H_2S (34.06 g mol^{-1}), respectively; V_m is the molar volume of H_2S at 1 atm and 25 °C (24.5 L mol^{-1}); C_{in} and C_{out} are the inlet and outlet concentration of H_2S (mg m^{-3}), *t* (h) is the reaction time for desulfurization. *TSC* is the theoretical sulfur capacity.

The used sorbent (denoted as S-sorbent) was regenerated in a 2.5 *vol.*% of O_2/N_2 gas mixture (165 mL min^{-1}) at 700 °C until no sulfur element formed or the concentration of SO_2 in the outlet gas cannot be detected by $KMnO_4$ solution. Schematic diagrams of the desulfurization process for hot coal gas and the synthetic spinel $ZnMn(Ce)_2O_4$/KIT-1 with double gyroidal mesopores were displayed in Fig. 1.

3. Results and discussions

3.1. BET characterization

N_2-adsorption isotherms and pore size distributions of KIT-1, fresh and used x%$ZnMn_2O_4$/KIT-1 sorbents were shown in Fig. 2, and all corresponding parameters of textural properties were given in Table 1. For KIT-1 support (Fig. 2A and C), its adsorption trend belonged to the type-IV isotherm with a sharp inflection at the relative pressure (p/p_0)
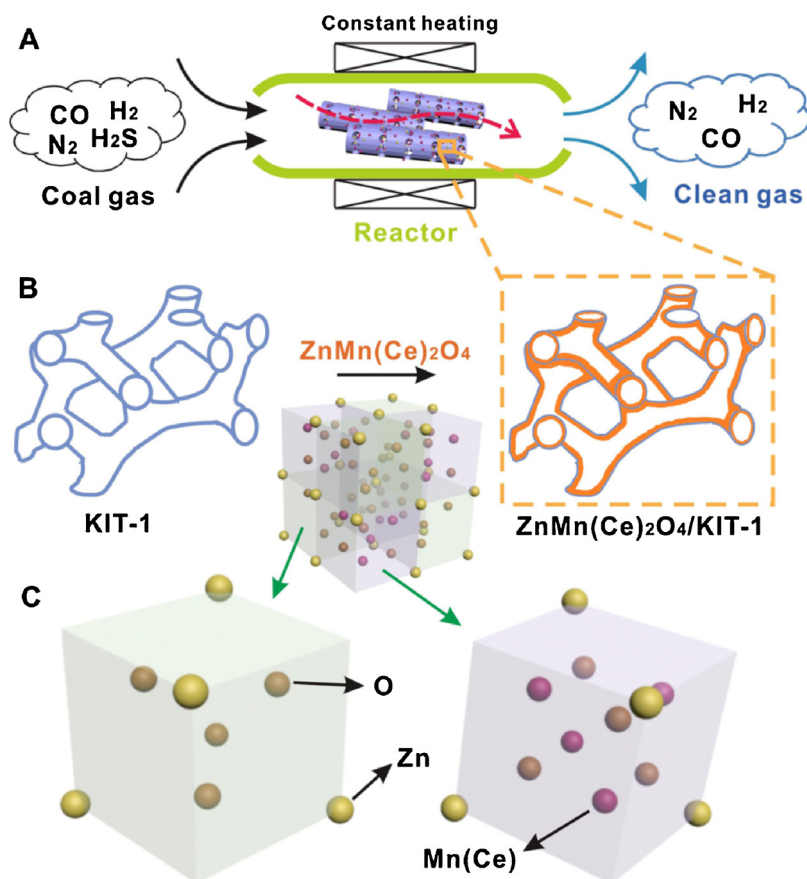
Fig. 1. Schematic diagrams of (A) desulfurization process for hot coal gas, (B) preparation of spinel $ZnMn(Ce)_2O_4$/KIT-1 and (C) $ZnMn(Ce)_2O_4$ spinel structure involving two typical cubic units.

range of 0.4-0.45. Such a profile was the characteristic of capillary condensation within uniform mesopore [33]. Whether it was specific surface area (S_{BET}) or total pore volume (V_p), KIT-1 had the better structure of double gyroidal mesopores for the loadings of active species than ZSM-5 [34]. But both S_{BET} and V_p values were decreased after $ZnMn_2O_4$ loading on KIT-1, ascribing to a partial blocking of KIT-1 channel. In particular, the incremental $ZnMn_2O_4$ content aggravated this downward trend, because the extent of partial blockage in pore was intensified. The shape of N_2-adsorption isotherm curves presented no obvious change (Fig. 2B), which indicated that the order structure of KIT-1 was still retained in these sorbents. Owing to the added $ZnMn_2O_4$ occupied the part space of channel, pore distributions of sorbents became broad and pore diameters decreased slightly (Fig. 2D). The low values of S_{BET} and V_p were detected obviously on 55%$ZnMn_2O_4$/KIT-1 sample, as the large clusters might be formed through the

agglomeration of individual nanoparticles. After desulfurization, KIT-1 still kept mesostructure in used sorbents, whose S_{BET} and V_p turned to small resulted from metal sulfide particles with a large molecule size. However, the values of S_{BET} and V_p decreased significantly at 650 °C compared with $ZnMn_2O_4$/KIT-1 used at other low temperature. The decline of surface area correlated closely with the sintering of active species at high temperature, because KIT-1 had a thermal stability even at 1000 °C according to the previous report [35]. Among the sorbents mixed with rare earth oxides (Fig. S1 in Supplementary materials), 45% $ZnMn(Ce)_2O_4$/KIT-1 had higher values of S_{BET} and V_p than others, revealing that CeO_2 could promote the dispersion of active species very well and against crystal growth during the preparation of sorbent [36].
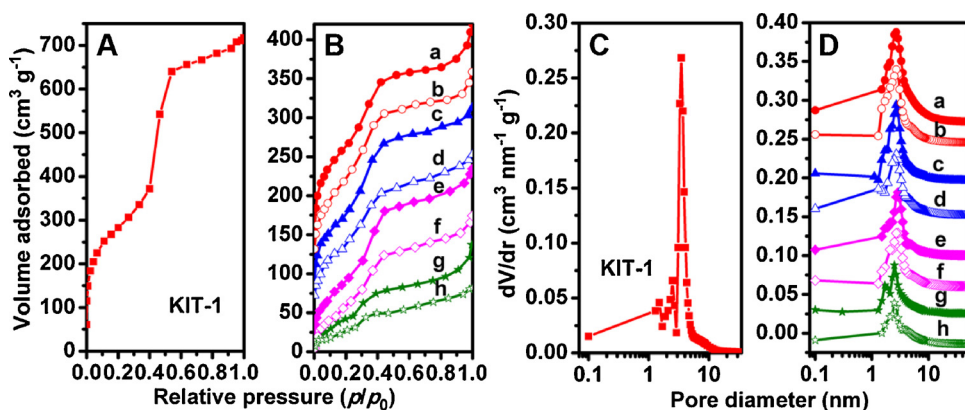

Fig. 2. (A, B) Nitrogen adsorption isotherms and (C, D) pore size distributions of pure KIT-1 and x%$ZnMn_2O_4$/KIT-1 sorbents before and after desulfurization. (a) 25%$ZnMn_2O_4$/KIT-1, (b) S-25%$ZnMn_2O_4$/KIT-1; (c) 35%$ZnMn_2O_4$/KIT-1, (d) S-35%$ZnMn_2O_4$/KIT-1; (e) 45% $ZnMn_2O_4$/KIT-1, (f) S-45%$ZnMn_2O_4$/KIT-1; (g) 55%$ZnMn_2O_4$/KIT-1, (h) S-55%$ZnMn_2O_4$/KIT-1.

Table 1
Specific surface area (S_{BET}), total pore volume (V_p) mesopore volume (V_{meso}), micopo re volume (V_{mic}), average pore diameter (D_a) of KIT-1, ZnMn$_2$O$_4$/KIT-1 sorbents.

Sample	S_{BET} (m^2 g^{-1})	V_p (cm^3 g^{-1})	V_{mic} (cm^3 g^{-1})	V_{meso} (cm^3 g^{-1})	D_p (nm)
KIT-1	1001	0.997	0.350	0.647	3.9
25%ZnMn$_2$O$_4$/KIT-1	650	0.472	0.223	0.249	2.9
35%ZnMn$_2$O$_4$/KIT-1	514	0.378	0.156	0.222	2.9
45%ZnMn$_2$O$_4$/KIT-1	427	0.362	0.133	0.229	3.4
55%ZnMn$_2$O$_4$/KIT-1	215	0.208	0.062	0.146	3.8
S-25%ZnMn$_2$O$_4$/KIT-1	520	0.386	0.155	0.231	3.0
S-35%ZnMn$_2$O$_4$/KIT-1	423	0.317	0.129	0.188	3.0
S-45%ZnMn$_2$O$_4$/KIT-1	350	0.292	0.107	0.185	3.3
S-55%ZnMn$_2$O$_4$/KIT-1	153	0.136	0.046	0.090	3.6
45%ZnMn(La)$_2$O$_4$/KIT-1	362	0.311	0.106	0.205	2.4
45%ZnMn(Ce)$_2$O$_4$/KIT-1	415	0.281	0.108	0.173	3.1
45%ZnMn(Sm)$_2$O$_4$/KIT-1	366	0.277	0.117	0.160	2.7
S-45%ZnMn(La)$_2$O$_4$/KIT-1	319	0.250	0.100	0.140	3.1
S-45%ZnMn(Ce)$_2$O$_4$/KIT-1	350	0.275	0.110	0.165	3.1
S-45%ZnMn(Sm)$_2$O$_4$/KIT-1	331	0.200	0.087	0.113	2.4
S-45%ZnMn$_2$O$_4$/KIT-1-500 °C	349	0.296	0.114	0.182	3.4
S-45%ZnMn$_2$O$_4$/KIT-1-600 °C	322	0.267	0.098	0.169	3.3
S-45%ZnMn$_2$O$_4$/KIT-1-650 °C	237	0.218	0.076	0.142	3.6

3.2. XRD analysis of sorbents

Fig. 3A showed XRD patterns of fresh x%ZnMn$_2$O$_4$/KIT-1 sorbents with different ZnMn$_2$O$_4$ contents or rare earth oxides doping, and Fig. S2 (In Supplementary materials) displayed the crystallite sizes (d) of ZnMn$_2$O$_4$ spinel nanoparticles in different sorbents estimated by the Scherrer equation (d = κλ/βcosθ). Ko et al [26] reported that the spinel structure of ZnMn$_2$O$_4$ could be formed at a certain stoichiometric ratio (Zn/Mn = 1/2). But there was no evident proved the diffraction peaks of ZnO and MnO$_x$, except a few of ZnMn$_2$O$_4$, appeared in 25%ZnMn$_2$O$_4$/KIT-1 and 35%ZnMn$_2$O$_4$/KIT-1, and their particle sizes corresponding to (211) reflection were about 13.49 and 17.74 nm, respectively. This indicated that ZnMn$_2$O$_4$ nanoparticles were highly dispersed in KIT-1 channels with lower loading. The diffraction peaks of ZnMn$_2$O$_4$ [PDF#24-1133] at 2θ = 29.3°, 31.2°, 32.9°, 36.4°, 38.9°, 44.8°, 59.0°, 60.8°, were observed clearly on 45%ZnMn$_2$O$_4$/KIT-1 ($d \approx$ 19.19 nm), and these peaks became sharper in 55%ZnMn$_2$O$_4$/KIT-1 pattern. The incremental loadings made some larger ZnMn$_2$O$_4$ nanoparticles depositing on the external surface of KIT-1 channels. Furthermore, no diffraction peaks of rare earth oxides were observed on the XRD patterns of 45%ZnMn$_2$O$_4$/KIT-1 mixed with 5 wt.% of rare earth oxides. As for 45%ZnMn(La)$_2$O$_4$/KIT-1 and 45%ZnMn(Sm)$_2$O$_4$/

KIT-1, the profiles of ZnMn$_2$O$_4$ diffraction patterns were almost the same as 45%ZnMn$_2$O$_4$/KIT-1. However, its diffraction peaks became broader and weaker remarkably in 45%ZnMn(Ce)$_2$O$_4$/KIT-1 (Fig. 3A(f)), suggesting that the spinel nanoparticles of ZnMn(Ce)$_2$O$_4$ spinel were smaller (10.67 nm) than these in others. The result implied that CeO$_2$ adding into the sorbent could facilitate the dispersion of active species on KIT-1 in accordance with N$_2$-adsorption analysis due to the fact that the similar nature between Ce^{3+} and Mn^{3+} ions (amphiprotic oxides) favor the occurrence of crystal lattice replace.

Fig. 3B showed the XRD patterns of used sorbents. The samples of S-25%ZnMn$_2$O$_4$/KIT-1 and S-35%ZnMn$_2$O$_4$/KIT-1 had very weak reflections of metal sulfides and their crystallite sizes estimated from the plane of (200) were 21.94 and 30.68 nm, respectively. Instead, S-45%ZnMn$_2$O$_4$/KIT-1 and S-55%ZnMn$_2$O$_4$/KIT-1 had two main metal sulfides whose diffraction peaks were observed evidently at 2θ = 29.6°, 34.3°, 49.2°, 61.4° and 2θ = 26.4°, 28.1°, 29.9°, 46.5°, 55.2° fitted with MnS [PDF#65-6745] and Mn$_{0.6}$Zn$_{0.4}$S [PDF#32-0635], respectively. Therefore, the desulfurization mechanism could be inferred as follows:

$$ZnMn_2O_4 = Mn_2O_3 + ZnO \tag{3}$$

$$Mn_2O_3 + H_2 + 2H_2S = 2MnS + 3H_2O \tag{4}$$

$$2ZnMn_2O_4 + 2H_2 + 6H_2S = MnS + 5Mn_{0.6}Zn_{0.4}S + 8H_2O \tag{5}$$

Compared to these over fresh 45%ZnMn(Ce)$_2$O$_4$/KIT-1, the diffraction peaks of ZnMn$_2$O$_4$ over the 5th regenerated 45%ZnMn(Ce)$_2$O$_4$/KIT-1 were intensified due to the aggregation of ZnMn$_2$O$_4$ nanoparticles during consecutive desulfurization-regeneration cycles.

3.3. H$_2$-TPR measurement

As shown in Fig. 4A, the strong reduction peaks were observed in the range of 402–470 °C for 25–55%ZnMn$_2$O$_4$/KIT-1 and following reduction reaction could occur: ZnMn$_2$O$_4$ + 2H$_2$ = 2MnO + Zn + 2H$_2$O. According to the report [37], the reduction temperature of pure ZnO was 814 °C whereas the reduced peaks of La$_2$ZnO$_4$/SBA-15 appeared at 601 °C. Therefore, the reduction peaks at 300–500 °C can be attributed to the transform of Mn$_2$O$_3$ to Mn$_3$O$_4$ and then to MnO because MnO was high stable throughout the test temperature range [38], similar to the results (360 and 435 °C) observed over 50%Mn$_2$O$_3$/KIT-1 [39]. Different profile was emerged with different ZnMn$_2$O$_4$ size and smaller nanoparticles can be reduced at low temperature as reported by Arena et al [40]. One dispersion-overlapped peak could be observed when ZnMn$_2$O$_4$ content was low (25 and 35 wt.%), because ZnMn$_2$O$_4$ nanoparticles were smaller and highly dispersed on the inner surface of KIT-1. Continued to increase the ZnMn$_2$O$_4$ content, the reduction peak became sharp and shifted to high temperature range gradually. Additionally, a small shoulder peak emerged at 611 °C in H$_2$-TPR profile of 55%ZnMn$_2$O$_4$/KIT-1, which correlated closely with the reduction of large-size ZnMn$_2$O$_4$ nanoparticles existed on the external surface of KIT-1. After the rare earth oxide was added to ZnMn$_2$O$_4$/KIT-1 via crystal lattice replace, the measured TPR profiles were almost the same
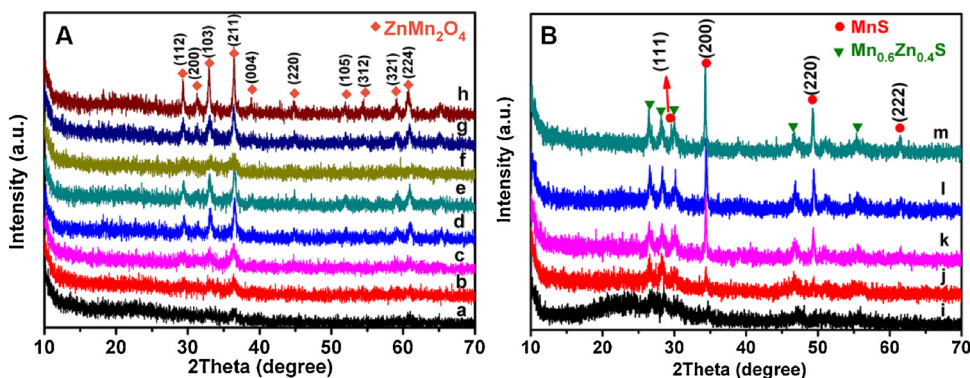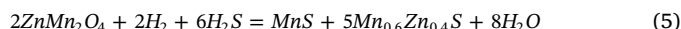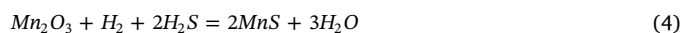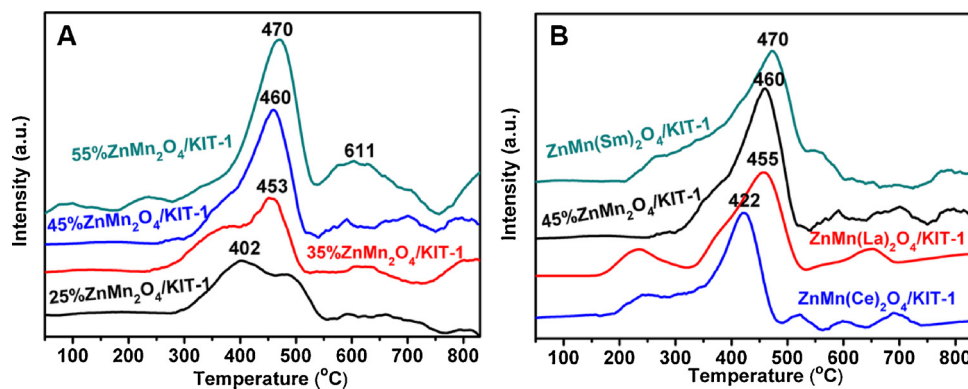

Fig. 3. Wide-angle XRD patterns of fresh, regenerated and used sorbents. (a, b, c, d) x% ZnMn$_2$O$_4$/KIT-1 (x = 25, 35, 45, 55); (e) 45% ZnMn(La)$_2$O$_4$/KIT-1; (f) 45%ZnMn (Ce)$_2$O$_4$/KIT-1; (g) 45%ZnMn(Sm)$_2$O$_4$/KIT-1; (h) 5th regenerated 45%ZnMn (Ce)$_2$O$_4$/KIT-1; (i, j, k, l) S-x%ZnMn$_2$O$_4$/KIT-1 (x = 25, 35, 45, 55); (m) S-45%ZnMn(Ce)$_2$O$_4$/KIT-1.

Fig. 4. H_2-TPR profile of x%ZnMn$_2$O$_4$/KIT-1 sorbents with (A) different ZnMn$_2$O$_4$ contents and (B) different rare earth oxide doping.

(Fig. 4B). However, the reduction peak of ZnMn$_2$O$_4$ shifted to low temperature (422 °C) over 45%ZnMn(Ce)$_2$O$_4$/KIT-1. This variation demonstrated that the size of ZnMn$_2$O$_4$ nanoparticles decreased remarkably, and CeO$_2$ was the more effective promoter of the ZnMn$_2$O$_4$ reducibility [41].

3.4. TG/DSC analysis

TG/DSC curves of S-45%ZnMn(Ce)$_2$O$_4$/KIT-1 at 550 °C were shown in Fig. 5. There are three exothermic peaks in DSC signals under the air condition (Fig. 5 DSC-a) and the first (367 °C) was corresponding to the formation of MnSO$_4$ [42]. As expected, we observed the corresponding weight-increased peak in TG curves. However, the increase weight (11.1%) was much lower than that expected value for a full conversion from MnS to MnSO$_4$ (M_{MnS} = 86.94 g mol^{-1} and M_{MnSO4} = 150.94 g mol^{-1}), i.e. 21.8% because partial of MnS was converted directly into Mn$_2$O$_3$ during the regeneration.

$$4Mns + 5O_2 = 2Mn_2O_3 + 4SO_2 \qquad (6)$$

It can be seen that the decomposition of MnSO$_4$ occurs at 550 °C accompanying with the decline of DSC curve. The second exothermic peak occurred at a higher temperature (637 °C) owing to the transformation from ZnS to ZnO, which was agreed with the previous report [43].

$$2ZnS + 3O_2 = 2ZnO + 2SO_2 \qquad (7)$$

Due to the decomposition of MnSO$_4$ to Mn$_2$O$_3$ and the transformation of ZnS to ZnO, the third exothermic peak around 743 °C in DSC curve was attributed to the formation of ZnMn$_2$O$_4$ spinel. In addition, TG/DSC curves of S-45%ZnMn(Ce)$_2$O$_4$ /KIT-1 treated under N$_2$ condition illustrated that there was not almost variation in the range of
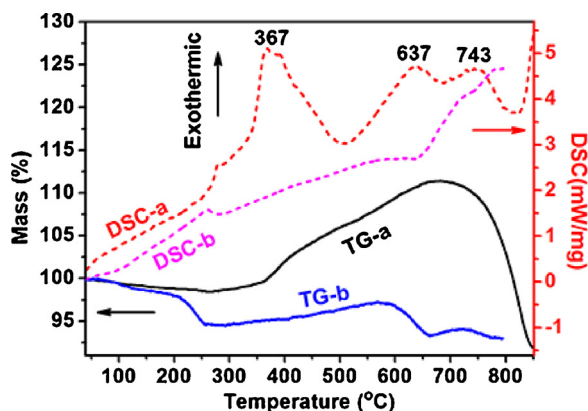

Fig. 5. TG/DSC profiles of 45%ZnMn(Ce)$_2$O$_4$/KIT-1 used at 550 °C. (a) air; (b) N$_2$.

800 °C except for a endothermic peak at ca. 260 °C due to the removal of adsorbed water. Slight weight gained in TG-b curve correlated closely with adsorbed oxygen in air.

3.5. HRTEM images of as-prepared KIT-1 and sorbents

The fine structures of as-prepared KIT-1, 45%ZnMn(Ce)$_2$O$_4$/KIT-1 and S-45%ZnMn(Ce)$_2$O$_4$/KIT-1 were fully investigated by means of HRTEM technique. As shown in Fig. 6A, as-prepared KIT-1 presented an ordered worm-like strip structure and its magnification image (Fig. 6B) verified that the distance between two bright and dark strips is ca. 3.71 nm, corresponding to the most-probable pore distribution of KIT-1 (Fig. 2C). After spinel ZnMn(Ce)$_2$O$_4$ nanoparticles loaded on the KIT-1 by a sol-gel procedure, the alternative strip structure of bright and dark still remained intact but these bright strips became narrower (inset in Fig. 6C), indicating that the ZnMn(Ce)$_2$O$_4$ particles formed on the internal surface, which was verified by the decline of most probable diameter (Fig. 2D) as well as average pore diameters (Table 1). In addition, EDS mapping in this region of ZnMn(Ce)$_2$O$_4$/KIT-1 revealed that elemental O, Si, Mn, Zn and Ce were distributed uniformly as bright spots in the channel of 45%ZnMn(Ce)$_2$O$_4$/KIT-1 although the resolution of elemental mappings was lower. Furthermore, the HRTEM images (Fig. 7) of ZnMn (Ce)$_2$O$_4$/KIT-1 before and after desulfurization illustrated that an ordered worm-like morphology remained intact, indicating that the ZnMn(Ce)$_2$O$_4$/KIT-1 sorbent presented excellent high temperature and hydrothermal stability, and part of large ZnMn(Ce)$_2$O$_4$ nanoparticles was also dispersed on the external surface of KIT-1. The inset in Fig. 7A showed the selected area electron diffraction (SAED) in this region, the light dots were dispersed disorderly on diffusion concentric circles, which indicated that ZnMn(Ce)$_2$O$_4$ with spinel structure existed mainly in polycrystalline particles with small amount of nanocrystallites. The crystal d-spacings estimated via the SAED patterns was corresponding to (211), (105) and (224) planes of ZnMn$_2$O$_4$ nanoparticles (Fig. 3A). The cross-section of ZnMn(Ce)$_2$O$_4$/KIT-1 channel was 2.36 nm in diameter, which was close to the most probable diameter (Fig. S1B(e)) and a magnification image can be seen clearly that the distances between two strips are 2.71 and 2.46 Å, respectively, corresponding to the d-spacings of (103) and (211) diffraction planes (nλ = 2dsinθ) of ZnMn(Ce)$_2$O$_4$ spinel structure (Fig. 7B). Another fine structure (Fig. 7C) of ZnMn(Ce)$_2$O$_4$ nanonanoparticles also demonstrated that the distances estimated between two strips were 2.02, 2.86 and 3.05 Å, which can be assigned to (220), (200) and (112) planes of ZnMn$_2$O$_4$ spinel on the surface. After desulfurization, the HRTEM image of S-ZnMn(Ce)$_2$O$_4$/KIT-1 (Fig. 7D) illustrated that the structure of used sorbent kept stable and the interplanar distance estimated by SAED pattern was in accordance with the (111), (220) and (200) d-spacing of MnS species (Fig. 3B). The magnification images of S-ZnMn(Ce)$_2$O$_4$/KIT-1 revealed that the presence of near-spherical shadows (2.28 or 3.15 nm) originated possibly from the channel of KIT-1 when the

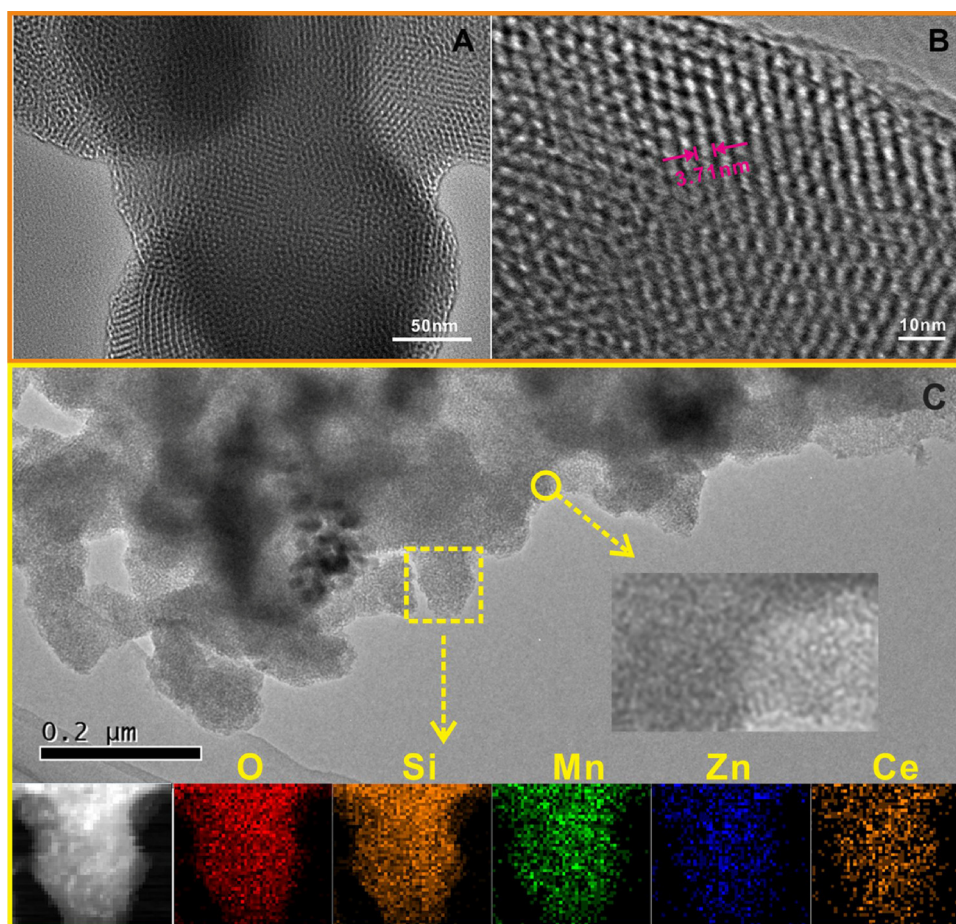Fig. 6. HRTEM images of (A, B) KIT-1, (C) ZnMn(Ce)$_2$O$_4$/KIT-1 and relative elemental mapping.

electron beam was parallel to pore direction (Fig. 7E, F). In the meantime, MnS and Mn$_{0.6}$Zn$_{0.4}$S species were detected within aforementioned shadows as well as on the surface of S-ZnMn(Ce)$_2$O$_4$/KIT-1. The existence of MnS and Mn$_{0.6}$Zn$_{0.4}$S nanocrystallites with the interplanar spacings of 1.85 Å (220), 3.02 Å (111) and 2.98 Å confirmed the transformation of metal oxides to sulfides.

3.6. SEM and EDS characterizations

To clarify the morphology and composition of sorbent, high resolution SEM image of 45%ZnMn(Ce)$_2$O$_4$/KIT-1 with EDS analysis was shown in Fig. 8. It can be seen that 45%ZnMn(Ce)$_2$O$_4$/KIT-1 presents the worm-like morphology with a diameter of 100 nm (Fig. 8A). The result of EDS analysis indicated that the molar ratio of Mn(Ce)/Zn was close to 2, which was in accordance with stoichiometric value of ZnMn(Ce)$_2$O$_4$ spinel. Moreover, the morphology and elemental composition of S-ZnMn(Ce)$_2$O$_4$/KIT-1 were shown in Fig. S3 (In Supplementary materials). It can be seen that there are a large amount of elemental sulfur (12.06 *at*.%) emerged over S-ZnMn(Ce)$_2$O$_4$/KIT-1 compared to fresh ZnMn(Ce)$_2$O$_4$/KIT-1 (Fig. 8B). the elemental mapping analysis indicated that every element distributed uniformly in the worm-like model, especially for Mn and Zn, which verified that there was not the migration and sinter of ZnMn(Ce)$_2$O$_4$ spinel nanoparticle appeared after desulfurization due to synergistic effect between ZnMn(Ce)$_2$O$_4$ spinel and KIT-1 support.

3.7. XPS analysis

In order to further make certain the elemental composition and valence status, ZnMn$_2$O$_4$/KIT-1, ZnMn(Ce)$_2$O$_4$/KIT-1 and S-ZnMn(Ce)$_2$O$_4$/KIT-1 sorbents were investigated by XPS technique. The peaks of O 1 s, C 1 s, Si 2p, Mn 2p and Zn 2p were observed in the total survey spectra (Fig. 9A), except for a weak XPS spectrum of Ce 3d for ZnMn$_2$O$_4$/KIT-1 and ZnMn(Ce)$_2$O$_4$/KIT-1. After desulfurization, the only difference was that the signal S 2p appeared in XPS spectrum of S-ZnMn(Ce)$_2$O$_4$/KIT-1 and a high-resolution XPS spectrum of S 2p at 162.4 eV was shown in Fig. 9C, which meant that the procedure of O/S exchange occurred. The high-resolution XPS spectra of O 1 s could be deconvoluted into three peaks at 532.5, 530.9 and 529.6 eV, corresponding to Si-O, Zn-O or Ce-O, Mn-O, respectively (Fig. 9B). In addition, the O1 s XPS spectra at 530.9 and 529.6 eV in intensity for S-ZnMn(Ce)$_2$O$_4$/KIT-1 became weaker due to the transformation of metal oxides to sulfides, indicated that the active species of ZnMn(Ce)$_2$O$_4$/KIT-1 was not fully utilized during desulfurization. Fig. 9D listed the elemental contents on the surface of ZnMn(Ce)$_2$O$_4$/KIT-1 before and after H$_2$S removal. The molar ratio of Si/O in ZnMn(Ce)$_2$O$_4$/KIT-1 was close to 1/2 except for O in metal oxides, implicating that the pore-wall of KIT-1 consists of SiO$_2$. The molar contents of Zn (1.5 *at*.%, 2.99 *at*.%) were close to these (1.62 *at*.%, 3.24 *at*.%) of Mn in ZnMn(Ce)$_2$O$_4$/KIT-1 and ZnMn$_2$O$_4$/KIT-1, respectively due to Zn^{2+} migration from the bulk to the surface. In contrast, the decline of Mn content in S-ZnMn(Ce)$_2$O$_4$/KIT-1 revealed that the attachment of S (2.13 *at*.%) further covered Mn and Ce. Moreover, the high-resolution XPS spectra of Si 2p, Mn 2p, Zn 2p and Ce 3d were depicted in Fig. S4 (in Supplementary materials). It can be seen that the binding energies (BEs) of Si 2p for fresh ZnMn$_2$O$_4$/KIT-1 and ZnMn(Ce)$_2$O$_4$/KIT-1 are 103.3 eV (Fig. S4 A(a,b)) whereas the BE of Si 2p for S-ZnMn(Ce)$_2$O$_4$/KIT-1 was 103.0 eV, which meant that the occurrence of O/S exchange during desulfurization would result in the change of silicon environment due to the strong interaction between ZnMn(Ce)$_2$O$_4$ nanoparticles and HO-Si groups on the inner

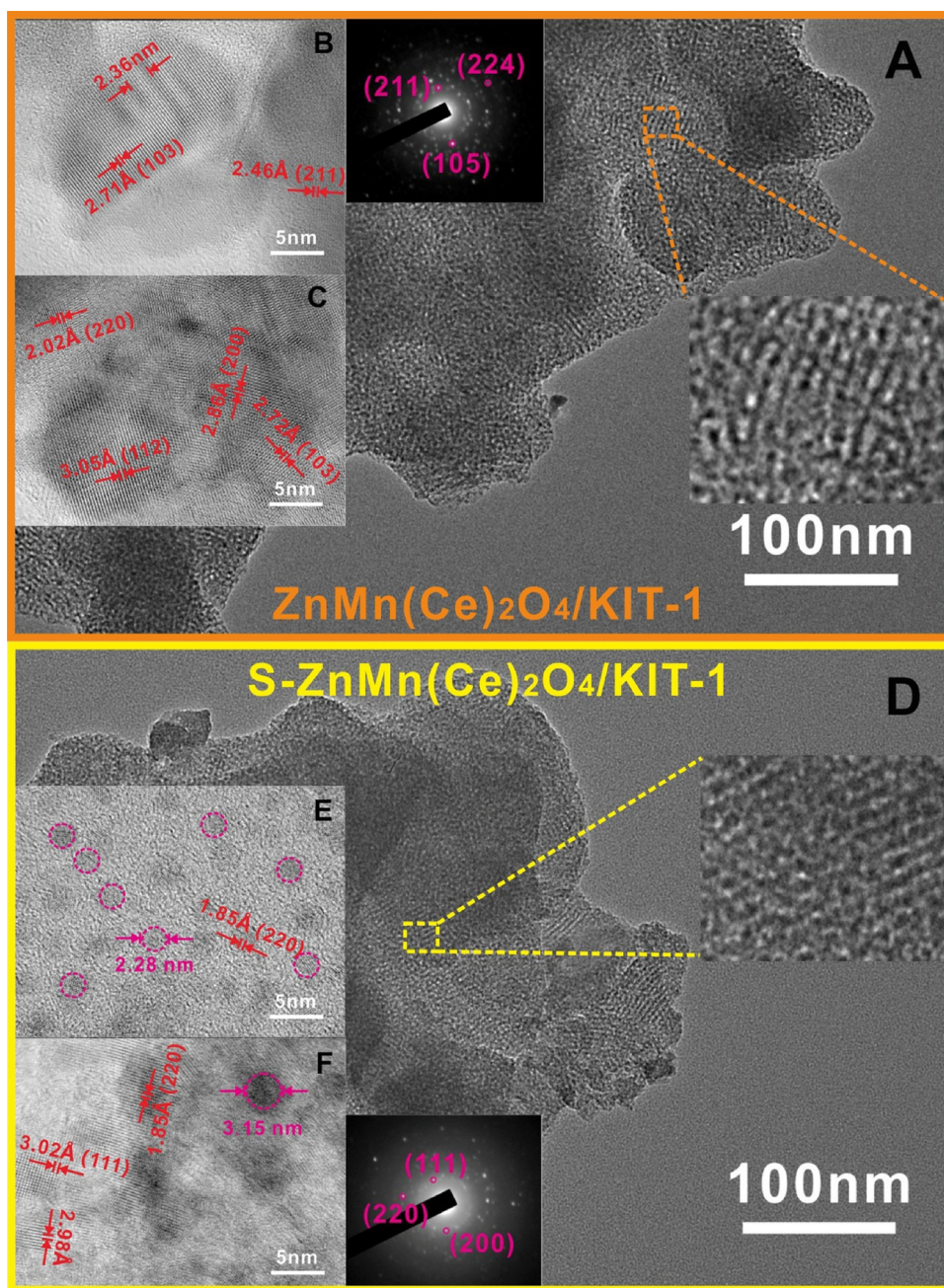**Fig. 7.** HRTEM images and SAED patterns of (A–C) 45%ZnMn(Ce)$_2$O$_4$/KIT-1 and (D–F) S-45%ZnMn(Ce)$_2$O$_4$/KIT-1.
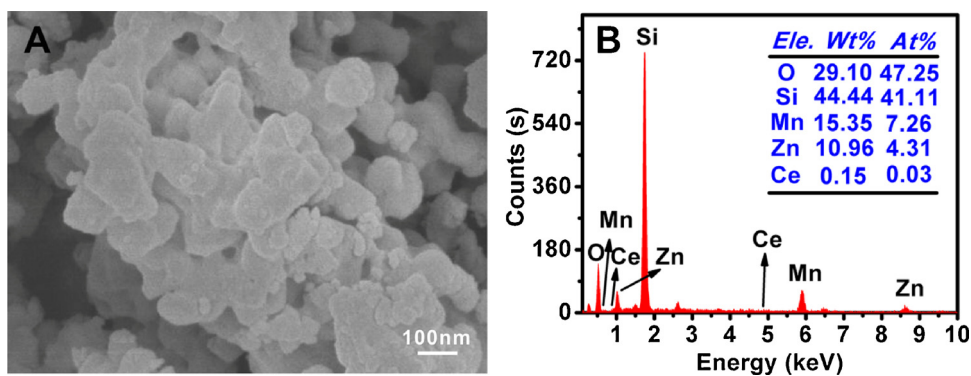

Fig. 8. (A) SEM image and (B) EDS spectrum of 45%ZnMn(Ce)$_2$O$_4$/KIT-1.
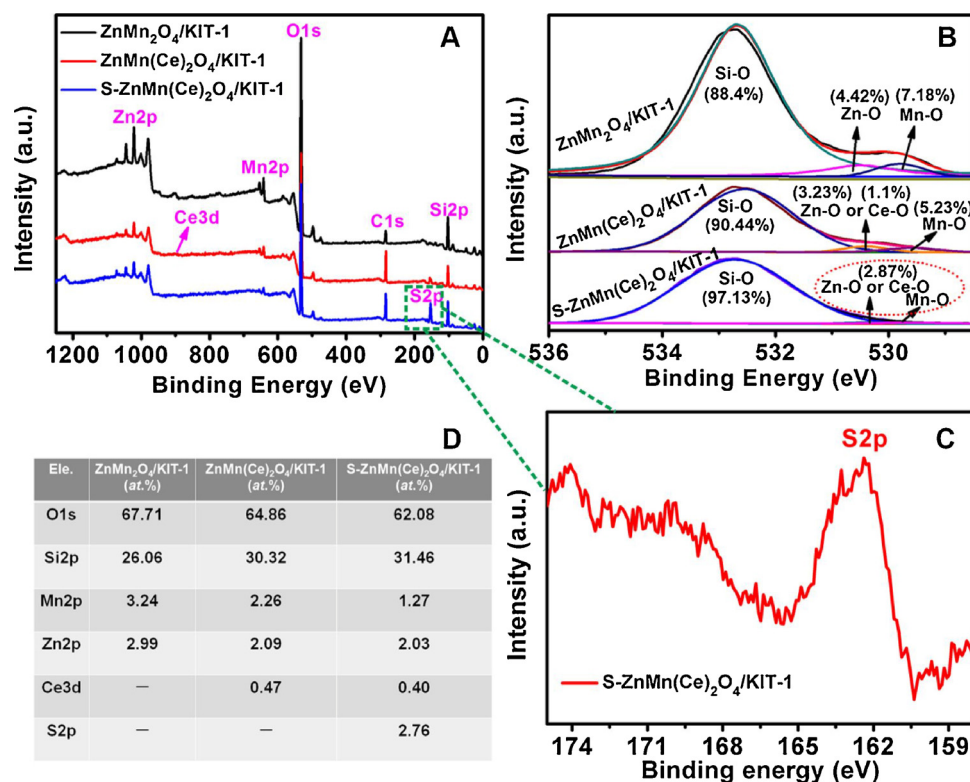
Fig. 9. Total XPS survey spectra and (B) O1 s high-resolution spectra of $ZnMn_2O_4$/KIT-1, $ZnMn(Ce)_2O_4$/KIT-1 and S-$ZnMn(Ce)_2O_4$/KIT-1, (C) S 2p high-resolution spectrum of S-$ZnMn(Ce)_2O_4$/KIT-1, (D) surface elemental composition.
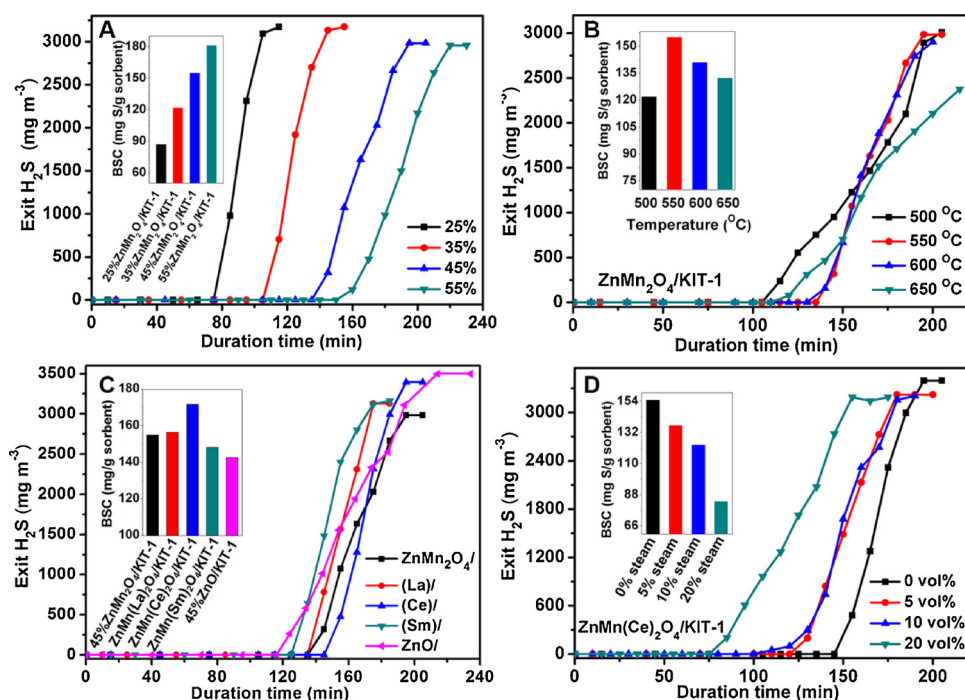
Ele.	$ZnMn_2O_4$/KIT-1 (at.%)	$ZnMn(Ce)_2O_4$/KIT-1 (at.%)	S-$ZnMn(Ce)_2O_4$/KIT-1 (at.%)
O1s	67.71	64.86	62.08
Si2p	26.06	30.32	31.46
Mn2p	3.24	2.26	1.27
Zn2p	2.99	2.09	2.03
Ce3d	—	0.47	0.40
S2p	—	—	2.76

Fig. 10. Desulfurization behavior over $ZnMn_2O_4$/KIT-1 and ZnO/KIT-1 sorbents at different condition ($GHSV = 2 \times 10^4$ mL h^{-1} g^{-1}; feed composition: 0.33% H_2S, 18% CO and N_2 balance gas). (A) Effect of $ZnMn_2O_4$ content ($T = 550$ °C); (B) effect of desulfurization temperature; (C) effect of rare earth oxides doping ($T = 550$ °C); (D) effect of steam volume ($T = 550$ °C). The insets are *BSC* values.

surface of KIT-1. Moreover, the BE of Mn $2p_{3/2}$ in $ZnMn_2O_4$/KIT-1 was 641.8 eV, slight higher than that (641.5 eV) of Mn $2p_{3/2}$ in $CoMn_2O_4$ [44]. However, the BE (642.0 eV) of Mn $2p_{3/2}$ in $ZnMn(Ce)_2O_4$/KIT-1 slight increased due to crystal lattice replace between Ce^{3+} and Mn^{3+}, which was more stable and more $Mn_{0.6}Zn_{0.4}S$ species were formed (Fig. 3B(m)) during desulfurization. There was almost not variation for Zn $2p_{3/2}$ XPS spectra of three sorbents before and after desulfurization. The XPS spectrum of Ce 3d was generally complex and only the state of

u_1 (904.5 eV) was observed here due to low CeO_2 loadings, belonging to unique photoelectron feature of the Ce^{3+} state [45]. In a word, the sulfur had been successfully retained in S-$ZnMn(Ce)_2O_4$/KIT-1 body.

3.8. FT-IR analysis

The FT-IR spectra of KIT-1, $ZnMn(Ce)_2O_4$/KIT-1 and S-$ZnMn$ $(Ce)_2O_4$/KIT-1 were shown in Fig. S5 (In Supplementary Materials). The

Table 2
Utilization of x%ZnMn$_2$O$_4$/KIT-1 sorbents with different ZnMn$_2$O$_4$ contents.

Sorbents	BSC (mg S/g sorbent)	TSC (mg S/g sorbent)	SU (%)
25%ZnMn$_2$O$_4$/KIT-1	88.1	100.3	87.8
35%ZnMn$_2$O$_4$/KIT-1	123.9	140.4	86.8
45%ZnMn$_2$O$_4$/KIT-1	155.0	180.5	85.9
55%ZnMn$_2$O$_4$/KIT-1	181.1	220.7	81.5

major peak located at around 3243 cm^{-1} was assigned to O−H stretching vibration of structural water in sorbent. The absorption bands at 1632 and 968 cm^{-1} were attributed to the Si−−OH bending and stretching vibrations. Likewise, the peaks at 1096, 798 and 473 cm^{-1} were ascribed to symmetric and asymmetric stretching vibrations as well as the Si−O−Si bending vibrations of KIT-1 [46]. It is noteworthy that a small peak observed at 621 cm^{-1} in the spectrum of ZnMn(Ce)$_2$O$_4$/KIT-1 was attributed to the blending vibration of metal oxides, which was shifted to 609 cm^{-1} in S-ZnMn(Ce)$_2$O$_4$/KIT-1 due to part of ZnMn(Ce)$_2$O$_4$ was converted to MnS and Mn$_{0.6}$Zn$_{0.4}$S in desulfurization reaction [47].

3.9. Desulfurization performances of sorbents

3.9.1. Effect of ZnMn$_2$O$_4$ spinel content

Preliminary desulfurization studies on ZnMn$_2$O$_4$/KIT-1 sorbents were carried out at 550 °C by varying ZnMn$_2$O$_4$ contents. The H$_2$S breakthrough curves and the corresponding BSC of 25%–55% ZnMn$_2$O$_4$/KIT-1 were presented in Fig. 10A, and all data were tabulated in Table 2. The incremental BSC and decreased SU were related to the increase of ZnMn$_2$O$_4$ contents in test range. More than 85% of SU was achieved over 25%–45%ZnMn$_2$O$_4$/KIT-1 except for 55%ZnMn$_2$O$_4$/KIT-1. Kinetic studies on the solid-phase reaction between H$_2$S and ZnMn$_2$O$_4$ indicated that desulfurization process occurred underwent a strong diffusion limitation [39,48]. Because high surface area as well as good dispersion of ZnMn$_2$O$_4$ was gained when the loading content was less than 55 wt.%. If the content upped to 55 wt.%, the available S_{BET} of ZnMn$_2$O$_4$/KIT-1 decreased due to the fact that some large ZnMn$_2$O$_4$ nanoparticles couldn't enter KIT-1 channels and formed their outside. The mass transfer resistance was increased with the formation of dense MnS and Mn$_{0.6}$Zn$_{0.4}$S layer in desulfurization process. It was hard to make use of the inner active species of channel for H$_2$S removal. Meanwhile, double gyroidal mesopores of KIT-1 played an important role in the reduction of internal diffusion resistance of H$_2$S, which made H$_2$S gas in full contact with the loaded ZnMn$_2$O$_4$ nanoparticles based on the high flow volume of channel in agreement with the BET and XRD results [37]. Out of large spinel nanoparticles accumulated on the outside of KIT-1 pores, 55%ZnMn$_2$O$_4$/KIT-1 possessed a low SU and the shape of breakthrough curve became smooth after the breakthrough point exceeded. As the moderate active component load, 45% ZnMn$_2$O$_4$/KIT-1 with high BSC (155.0 mg S/g sorbent) and SU (85.9%) at 550 °C ought to be chosen for further desulfurization investigations.

3.9.2. Effect of desulfurization temperature

Fig. 10B displayed that H$_2$S breakthrough curves and BSC over 45% ZnMn$_2$O$_4$/KIT-1 at different temperature (500–650 °C). Remarkably, 45%ZnMn$_2$O$_4$/KIT-1 sorbent at a test temperature of 550 °C exhibited the best desulfurization behavior with longer breakthrough time. Meanwhile, its BSC value was 155.0 (mg S/g sorbent) which was higher than that of other temperatures. Thermodynamic calculation inferred that high temperature was beneficial to accelerate the exchange rate of S/O in Mn-based sorbent. Only the surface sites of Mn-based sorbent, except for other unusable sites in sub-surface and inner layer, could be utilized at low temperature. Therefore, 45%ZnMn$_2$O$_4$/KIT-1 exhibited the lowest sulfur capacity at 500 °C. According to the H$_2$-TPR results, Zn^{2+} in 45%ZnMn$_2$O$_4$ spinel was probably reduced to elemental Zn and

vaporized during the desulfurization (> 600 °C), which could be detected clearly on the reactor outlet, leading to the loss of active components under the strong reducing atmosphere [26]. It is noticeable that 550 °C was the reasonable temperature on removal of H$_2$S by 45% ZnMn$_2$O$_4$/KIT-1, because this temperature could maintain the Zn^{2+} stability without being reduced before the vulcanization of 45% ZnMn$_2$O$_4$ spinel.

3.9.3. Effect of rare earth oxides doping

Many studies reported that the addition of another metal, especially the rare earth elements, could further enhance the sorbent stability and increase its BSC by the synergetic effect in mixture phase [49]. In this work, three kinds of rare earth oxides (La$_2$O$_3$, CeO$_2$ and Sm$_2$O$_3$) were blended to mix into the 45%ZnMn$_2$O$_4$/KIT-1, and desulfurization performances of new sorbents were evaluated at 550 °C. Although the rare earth oxide content was only 5 wt.%, a notable difference in H$_2$S removal appeared at the same condition. Fig. 10C clearly noted that the BSC (142.6 mg S/g sorbent) over 45%ZnO/KIT-1 was relatively lower and the breakthrough curve became smooth after breakthrough point, which meant that the formation of dense ZnS layer on the surface of 45%ZnO/KIT-1 limited the diffusion of H$_2$S molecules from surface to the bulk whereas the BSC over ZnMn$_2$O$_4$/KIT-1 enhanced remarkably due to high dispersion of ZnMn$_2$O$_4$ spinel nanoparticles. Moreover, ZnMn(Ce)$_2$O$_4$/KIT-1 had the excellent desulfurization capacity (171.7 mg S/g sorbent) and steeper increase of adsorption breakthrough curve, owing to the highly dispersed ZnMn(Ce)$_2$O$_4$ nanoparticles which were formed by Ce^{3+} ions occupying the positions of Mn^{3+} in cubic lattice of spinel over KIT-1 pores via crystalline substitution. The BSC of ZnMn(La)$_2$O$_4$/KIT-1 (156.5 mg S/g sorbent) was not increased remarkably compared with the pure 45%ZnMn$_2$O$_4$/KIT-1 (155.0 mg S/g sorbent), but its deactivate rate curve became very steep after the breakthrough point. This inferred that the dispersion of ZnMn$_2$O$_4$ after doping with La was improved slightly. However, the BSC of ZnMn(Sm)$_2$O$_4$/KIT-1 (148.3 mg S/g sorbent) was obviously lower than the undoped ZnMn$_2$O$_4$/KIT-1, owing to the removal ability of Sm$_2$O$_3$ for H$_2$S at high temperature was poor and thus its capacity could be neglected [50]. Besides, the mass transmission on the removal of H$_2$S by ZnMn(Sm)$_2$O$_4$/KIT-1 was also resisted with the decreased Vp (Table 1). Indeed, the order of doping effect of rare earth oxide on ZnMn$_2$O$_4$/KIT-1 desulfurization was CeO$_2$ > La$_2$O$_3$ > Sm$_2$O$_3$.

3.9.4. Effect of steam contents in hot coal gas

Hot coal gas containing high steam can be generated during the coal gasification which severely hinders the desulfurization reaction [51]. Therefore, it is crucial to design a high-performance sorbent that can suppress the reaction with steam in hot coal gas. The desulfurization behavior of ZnMn(Ce)$_2$O$_4$/KIT-1 was investigated under the conditions of steam conditions. As shown in Fig. 10D, the BSC of ZnMn(Ce)$_2$O$_4$/KIT-1 was the highest (171.7 mg S/g sorbent) without steam. However, BSC decreased remarkably with an incremental steam contents from 5 vol.% to 20 vol.%. When the presence of steam was 5 vol.% and 10 vol.%, the BSC over ZnMn(Ce)$_2$O$_4$/KIT-1 was still 137.1 and 123.4 mg S/g sorbent, respectively. If the steam content reached to 20 vol.% in feed gas, there were only BSC of 83.4 mg S/g sorbent over ZnMn(Ce)$_2$O$_4$/KIT-1, which meant that almost 52% of initial sulfur capacity was retained. According to XRD results (Fig. 3A), the main crystal phase in ZnMn(Ce)$_2$O$_4$/KIT-1 sorbent for desulfurization accompanying with the reaction (4, 5) was ZnMn$_2$O$_4$ spinel. The equilibrium constant of the reaction could be described as follows:

$$K_{eq} = [MeS][H_2O]/[MeO][H_2S] \; (Me = Zn, Mn) \qquad (8)$$

From the kinetic studies, the desulfurization efficiency as well as BSC value would decrease distinctly when the steam content increased [52]. In our previous work, 4Mn1Ce/HMS sorbent had an obvious decrease of BSC (55 mg S/g sorbent) at 600 °C when feed gas contained
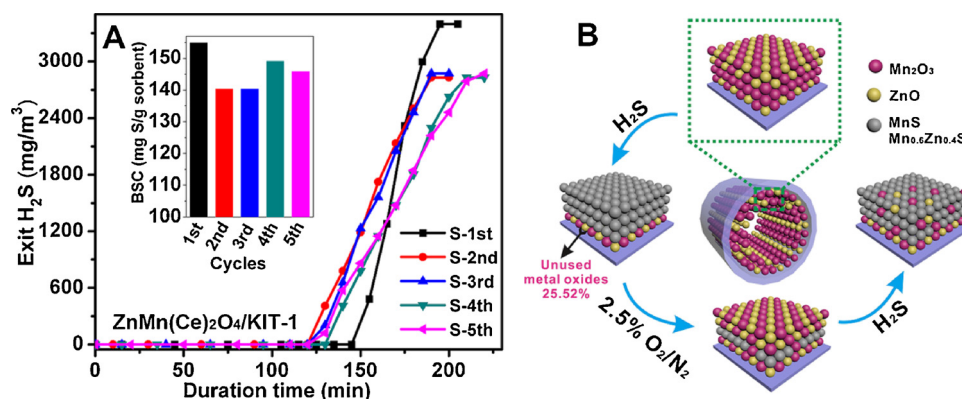
Fig. 11. (A) H_2S breakthrough curves and (B) schematic diagram of desulfurization-regeneration cycles over $ZnMn(Ce)_2O_4$/KIT-1 ($GHSV = 2 \times 10^4$ mL h^{-1} g^{-1}; T. = 550 °C; $T_{Reg.}$ = 700 °C; feed composition: 0.33% H_2S, 10.6% H_2, 18% CO and N_2 balance gas).

7% steam [22]. Compared with pure Mn_3O_4 in 4Mn1Ce/HMS, the mixed spinel structure of $ZnMn_2O_4$ in $ZnMn(Ce)_2O_4$/KIT-1 was insensitive for the deactivation caused by steam (or the formation of stable $Mn_{0.6}Zn_{0.4}S$ species) on account of large desulfurization equilibrium constant of ZnO. Additionally, the Ce^{3+} ions located Mn^{3+} sites reacted with H_2S to form high-stable Ce_2O_2S species which will restrict the reversible reaction with water vapor despite of low BSC for Ce_2O_3 [51]. The competitive adsorption between H_2S and H_2O on the surface sites of $ZnMn(Ce)_2O_4$/KIT-1 was not such apparent as other pure Mn-based sorbents. Low steam content in hot coal gas did not seem to have a significant effect on H_2S uptake by $ZnMn(Ce)_2O_4$/KIT-1 sorbent.

3.9.5. Successive desulfurization-regeneration cycles

$MnSO_4$ may appear during the regeneration of Mn-based sorbent and it could not be deposition before 700 °C [53]. Therefore, the reusability of $ZnMn(Ce)_2O_4$/KIT-1 was detected in five consecutive cycles of desulfurization (550 °C) and regeneration (700 °C). Compared with the original sorbent, *BSC* were reduced slightly in the second use and continued to change with time increasing (Fig. 11A). After five successful cycles, $ZnMn(Ce)_2O_4$/KIT-1 still showed a high sulfur capacity (145.9 mg S/g sorbent) as upped to 85% of its initial value which was higher than Zn-Mn sorbents supported on SiO_2 (19.8 mg S/g sorbent) [26]. Because highly homogeneous dispersion of elements in double gyroidal mesopores of KIT-1 still kept their stable distribution state after desulfurization in accordance with EDS maps of S-$ZnMn(Ce)_2O_4$/KIT-1 (Fig. S3, in Supplementary materials). But for the decreased desulfurization capacity after use, one reason was that $ZnMn_2O_4$ particle size in the fifth regenerated $ZnMn(Ce)_2O_4$/KIT-1 turned to larger than fresh sorbent owing to particle aggregations at the high regeneration temperature (Fig. 3A(h)). Another was that a part of $ZnMn(Ce)_2O_4$ which couldn't be recovered in oxidative atmosphere, will be the inactive sites that couldn't re-play the desulfurization feature (Fig. 11B). It was remarkable that the mole of the remaining active species of $ZnMn(Ce)_2O_4$/KIT-1 surface unused in the first desulfurization was about 25.52% from the molar mass calculation of XPS results. With the results above, $ZnMn(Ce)_2O_4$/KIT-1 possessed excellent regenerated nature with basically constant sulfur capacity.

4. Conclusions

A series of $ZnMn_2O_4$/KIT-1 sorbents were synthesized by $ZnMn_2O_4$ spinel loading on KIT-1 support with 3-dimensional wormhole-like channels and further doped with rare earth oxides for hot coal gas desulfurization. The double gyroidal mesopores of KIT-1 provided a larger specific area (1001 m^2 g^{-1}) for the inner mass transmission of H_2S and improved the sorbent stability. The XRD results confirmed that the successfully prepared $ZnMn_2O_4$ spinel was converted to MnS and $Mn_{0.6}Zn_{0.4}S$ after desulfurization and crystal lattice replace between

Ce^{3+} and Mn^{3+} facilitated the dispersion of active species. High sorbent utilization (85%) was achieved when the $ZnMn_2O_4$ loading content over KIT-1 less than 55 *wt.*%. The formation of $ZnMn_2O_4$ spinel could significantly avoid Zn^{2+} converting to elemental Zn and reduced the Zn vaporization at high temperature. Doping a small amount of CeO_2 into $ZnMn_2O_4$/KIT-1 could facilitate $ZnMn_2O_4$ activity and decrease its particle size remarkably. Because $ZnMn_2O_4$ was insensitive to steam during desulfurization, the removal ability of $ZnMn(Ce)_2O_4$/KIT-1 for H_2S was still stable in different steam content. $ZnMn(Ce)_2O_4$/KIT-1 exhibited a high *BSC* (171.7 mg S/g sorbent) at 550 °C and performed a slight decay in capability after five successive desulfurization-regeneration cycles. In conclusion, spinel $ZnMn(Ce)_2O_4$/KIT-1 is a promising sorbent with double gyroidal mesopores for hot coal gas desulfurization at high temperature.

Appendix A. Supplementary data

Supplementary material related to this article can be found, in the online version, at doi:https://doi.org/10.1016/j.apcatb.2018.06.056.

References

[1] K. Chen, N. Liu, M. Zhang, D. Wang, Oxidative desulfurization of dibenzothiophene over monoclinic VO_2 phase-transition catalysts, Appl. Catal. B Environ. 212 (2017) 32–40.

[2] Y. Zhao, C. Wang, M. Liu, D. Chong, J. Yan, Improving operational flexibility by regulating extraction steam of high-pressure heaters on a 660 MW supercritical coal-fired power plant: a dynamic simulation, Appl. Energy 212 (2018) 1295–1309.

[3] C. Yang, H. Ji, C. Chen, W. Ma, J. Zhao, Desulfurization of thiophenes in oils into H_2SO_4 using molecular oxygen, Appl. Catal. B Environ. 235 (2018) 207–213, http://dx.doi.org/10.1016/j.apcatb.2018.04.076.

[4] M. Dan, Q. Zhang, S. Yu, A. Prakash, Y. Lin, Y. Zhou, Noble-metal-free MnS/In$_2$S$_3$ composite as highly efficient visible light driven photocatalyst for H_2 production from H_2S, Appl. Catal. B Environ. 217 (2017) 530–539.

[5] X. Zeng, X. Xiao, Y. Li, J. Chen, H. Wang, Deep desulfurization of liquid fuels with molecular oxygen through graphene photocatalytic oxidation, Appl. Catal. B Environ. 209 (2017) 98–109.

[6] Y. Zhang, B. Jin, X. Zou, H. Zhao, A clean coal utilization technology based on coal pyrolysis and chemical looping with oxygen uncoupling: principle and experimental validation, Energy 98 (2016) 181–189.

[7] T.A. DeNooyer, J.M. Peschel, Z. Zhang, A.S. Stillwell, Integrating water resources and power generation: the energy–water nexus in Illinois, Appl. Energy 162 (2016) 363–371.

[8] Y. Man, M. Hong, J. Li, S. Yang, Y. Qian, H. Liu, Paper mills integrated gasification combined cycle process with high energy efficiency for cleaner production, J. Clean. Prod. 156 (2017) 244–252.

[9] W. Shi, M. Han, A conceptual design of catalytic gasification fuel cell hybrid power

plant with oxygen transfer membrane, J. Power Sources 361 (2017) 211–220.

[10] D. Julião, A.C. Gomes, M. Pillinger, R. Valença, J.C. Ribeiro, I.S. Gonçalves, S.S. Balula, Desulfurization of liquid fuels by extraction and sulfoxidation using H_2O_2 and [CpMo(CO)3R] as catalysts, Appl. Catal. B Environ. 230 (2018) 177–183.

[11] D.B. Bukur, X. Lang, D. Mukesh, W.H. Zimmerman, M.P. Rosynek, C. Li, Binder/support effects on the activity and selectivity of iron catalysts in the Fischer-Tropsch synthesis, Ind. Eng. Chem. Res. 29 (1991) 1588–1599.

[12] F. Ju, C. Liu, K. Li, C. Meng, S. Gao, H. Ling, Reactive adsorption desulfurization of fluidized catalytically cracked (FCC) gasoline over a ca-doped Ni-ZnO/Al2O3–SiO2 adsorbent, Energy Fuel 30 (2016) 6688–6697.

[13] F. Ortloff, J. Bohnau, U. Kramar, F. Graf, T. Kolb, Studies on the influence of H_2S and SO_2 on the activity of a PdO/Al2O3 catalyst for removal of oxygen by total oxidation of (bio-)methane at very low O_2:CH_4 ratios, Appl. Catal. B Environ. 182 (2016) 550–561.

[14] Y. Li, Y. Feng, Q. Zhou, M. Wu, J. Mi, Effects of microwave irradiation on the structure of zinc oxide sorbents for high temperature coal gas desulfurization, Energy Fuel 31 (2017) 8512–8520.

[15] Y. Feng, J. Mi, M. Wu, J. Shangguan, H. Fan, In situ preparation and regeneration behaviors of zinc oxide/red clay desulfurization sorbents, Energy Fuel 31 (2017) 1015–1022.

[16] W.D. Oh, J. Lei, A. Veksha, A. Giannis, G. Lisak, V.W.C. Chang, X. Hu, T.T. Lim, Influence of surface morphology on the performance of nanostructured ZnO-loaded ceramic honeycomb for syngas desulfurization, Fuel 211 (2018) 591–599.

[17] L.R. Pahalagedara, A.S. Poyraz, W. Song, C.-H. Kuo, M.N. Pahalagedara, Y.-T. Meng, S.L. Suib, Low temperature desulfurization of H_2S: High sorption capacities by mesoporous cobalt oxide via increased H_2S diffusion, Chem. Mater. 26 (2014) 6613–6621.

[18] S. Chytil, M. Kure, R. Lødeng, E.A. Blekkan, Performance of Mn-based H_2S sorbents in dry, reducing atmosphere–Manganese oxide support effects, Fuel 196 (2017) 124–133.

[19] Y. Xu, Q. Zhong, X. Liu, Elemental mercury oxidation and adsorption on magnesite powder modified by Mn at low temperature, J. Hazard. Mater. 283 (2015) 252–259.

[20] H. Xia, B. Liu, Q. Li, Z. Huang, A.S.-C. Cheung, High capacity Mn-Fe-Mo/FSM-16 sorbents in hot coal gas desulfurization and mechanism of elemental sulfur formation, Appl. Catal. B Environ. 200 (2017) 552–565.

[21] K.M. Dooley, V. Kalakota, S. Adusumilli, High-temperature desulfurization of gasifier effluents with rare earth and rare earth/transition metal oxides, Energy Fuel 25 (2011) 1213–1220.

[22] Z.F. Zhang, B.S. Liu, F. Wang, J.F. Li, Fabrication and performance of xMnyCe/hexagonal mesoporous silica sorbents with wormhole-like framework for hot coal gas desulfurization, Energy Fuel 27 (2013) 7754–7761.

[23] C. Li, X. Han, F. Cheng, Y. Hu, C. Chen, J. Chen, Phase and composition controllable synthesis of cobalt manganese spinel nanoparticles towards efficient oxygen electrocatalysis, Nat. Commun. 6 (2015) 7345.

[24] Y. Li, Y. Li, Y. Yin, D. Xia, H. Ding, C. Ding, J. Wu, Y. Yan, Y. Liu, N. Chen, P.K. Wong, A. Lu, Facile synthesis of highly efficient ZnO/ZnFe2O4 photocatalyst using earth-abundant sphalerite and its visible light photocatalytic activity, Appl. Catal. B Environ. 226 (2018) 324–336.

[25] C.W. Cady, G. Gardner, Z.O. Maron, M. Retuerto, Y.B. Go, S. Segan, M. Greenblatt, G.C. Dismukes, Tuning the electrocatalytic water oxidation properties of AB2O4 spinel nanocrystals: a (Li, Mg, Zn) and B (Mn, Co) site variants of LiMn2O4, ACS Catal. 5 (2015) 3403–3410.

[26] T.H. Ko, H. Chu, Y.J. Liou, A study of Zn–Mn based sorbent for the high-temperature removal of H_2S from coal-derived gas, J. Hazard. Mater. 147 (2007) 334–341.

[27] Y.T. Lu, Y.J. Chien, C.F. Liu, T.H. You, C.C. Hu, Active site-engineered bifunctional electrocatalysts of ternary spinel oxides, M0.1Ni0.9Co2O4 (M: Mn, Fe, Cu, Zn) for the air electrode of rechargeable zinc-air batteries, J. Mater. Chem. A 5 (2017) 21016–21026.

[28] J. Chen, M. Wu, Z. Wu, H. Fan, J. Mi, Effects of microwave irradiation on H_2S removal activity from hot coal gas by modified semicoke-supported ZnO sorbents, J. Mater. Sci. 51 (2016) 2850–2858.

[29] Y.S. Hong, K.R. Sin, J.S. Pak, C.J. Kim, B.S. Liu, Kinetic analysis of H_2S removal over mesoporous Cu–Mn mixed oxide/SBA-15 and La–Mn mixed oxide/KIT-6 sorbents during hot coal gas desulfurization using the deactivation kinetics model, Energy Fuel 31 (2017) 9874–9880.

[30] Z.F. Zhang, B.S. Liu, F. Wang, W.S. Wang, C. Xia, S. Zheng, R. Amin, Hydrogen sulfide removal from hot coal gas by various mesoporous silica supported Mn2O3

[31] R. Ryoo, J.M. Kim, C.H. Ko, C.H. Shin, Disordered molecular sieve with branched mesoporous channel network, J. Phys. Chem. 100 (1996) 17718–17721.

[32] B.S. Liu, X.N. Wei, Y.P. Zhan, R.Z. Chang, F. Subhan, C.T. Au, Preparation and desulfurization performance of LaMeOx/SBA-15 for hot coal gas, Appl. Catal. B Environ. 102 (2011) 27–36.

[33] K. Cassiers, T. Linssen, M. Mathieu, M. Benjelloun, K. Schrijnemakers, P. Van Der Voort, P. Cool, E.F. Vansant, A detailed study of thermal, hydrothermal, and mechanical stabilities of a wide range of surfactant assembled mesoporous silicas, Chem. Mater. 14 (2002) 2317–2324.

[34] D. Liu, W. Zhou, J. Wu, CeO2–MnOx/ZSM-5 sorbents for H_2S removal at high temperature, Chem. Eng. J. 284 (2016) 862–871.

[35] H. Sanaeishoar, M. Sabbaghan, F. Mohave, R. Nazarpour, Disordered mesoporous KIT-1 synthesized by DABCO-based ionic liquid and its characterization, Microporous Mesoporous Mater. 228 (2016) 305–309.

[36] L.H. Ren, H.L. Zhang, A.H. Lu, Y. Hao, W.C. Li, Porous silica as supports for controlled fabrication of Au/CeO2/SiO2 catalysts for CO oxidation: influence of the silica nanostructures, Microporous Mesoporous Mater. 158 (2012) 7–12.

[37] Z. Wang, M. Flytzani-Stephanopoulos, Cerium oxide-based sorbents for regenerative hot reformate gas desulfurization, Energy Fuel 19 (2005) 2089–2097.

[38] W.D. Tang, J. Li, L. Sun, J. Hao, Origination of N_2O from NO reduction by NH_3 over β-MnO_2 and α-Mn_2O_3, Appl. Catal. B Environ. 99 (2010) 156–162.

[39] H.F. Garces, A.E. Espinal, S.L. Suib, Tunable shape microwave synthesis of zinc oxide nanospheres and their desulfurization performance compared with nanorods and platelet-like morphologies for the removal of hydrogen sulfide, J. Phys. Chem. C 116 (2012) 8465–8474.

[40] F. Arena, T. Torre, C. Raimondo, A. Parmaliana, Structure and redox properties of bulk and supported manganese oxide catalysts, Phys. Chem. Chem. Phys. 3 (2001) 1911–1917.

[41] R.S. Kempegowda, N. Laosiripojana, S. Assabumrungrat, High temperature desulfurization over nano-scale high surface area ceria for application in SOFC, Korean J. Chem. Eng. 25 (2008) 223–230.

[42] X.W. Xiang, Q. Peng, X. Wu, Y. Li, F. Tang, R. Song, Z. Liu, Z. He, X. Wu, Green-low-cost rechargeable aqueous zinc-ion batteries using hollow porous spinel ZnMn2O4 as the cathode material, J. Mater. Chem. A 5 (2017) 17990–17997.

[43] I. Perraud, R.M. Ayral, C. Cammarano, F. Rouessac, V. Hulea, A. Ayral, Sulfidation and sulfur capacity of fine ZnO powder derived from thermal oxidation of mechanosynthesized ZnS powder, Chem. Eng. J. 241 (2014) 360–365.

[44] M. Oku, K. Hirokawa, X-ray photoelectron spectroscopy of Co3O4, Fe3O4, Mn3O4, and related compounds, J. Electron. Spectrosc. 8 (1976) 475–481.

[45] R. Amin, X. Chang, B. Liu, Synergistic effect of CeO2 in CH_4/CO_2 dry reforming reaction over stable xCeO2 yNi/MCM-22 catalysts, Ind. Eng. Chem. Res. 56 (2017) 7445–7453.

[46] Y.H. Guo, C. Xia, B.S. Liu, Catalytic properties and stability of cubic mesoporous LaxNiyOz/KIT-6 catalysts for CO_2 reforming of CH_4, Chem. Eng. J. 237 (2014) 421–429.

[47] B. Wei, L. Meng, H. Li, C. Yao, Q. Han, Facile synthesis of MnOxS2−x nanofiber arrays films on Ti for performance supercapacitor application, J. Alloy Compd. 721 (2017) 285–290.

[48] H.L. Fan, T. Sun, Y.P. Zhao, J. Shangguan, J.Y. Lin, Three-dimensionally ordered macroporous iron oxide for removal of H_2S at medium temperatures, Environ. Sci. Technol. 47 (2013) 4859–4865.

[49] M. Flytzani-Stephanopoulos, M. Sakbodin, Z. Wang, Regenerative adsorption and removal of H_2S from hot fuel gas streams by rare earth oxides, Science 312 (2006) 1508–1510.

[50] B.S. Liu, Z.Y. Wan, F. Wang, Y.P. Zhan, M. Tian, A.S.C. Cheung, $^{18}O_2$ label mechanism of sulfur generation and characterization in properties over mesoporous Sm-based sorbents for hot coal gas desulfurization, J. Hazard. Mater. 267 (2014) 229–237.

[51] M. Asadullah, Biomass gasification gas cleaning for downstream applications: a comparative critical review, Renew. Sustain. Energy Rev. 40 (2014) 118–132.

[52] S. Cheah, Y.O. Parent, W.S. Jablonski, T. Vinzant, J.L. Olstad, Manganese and ceria sorbents for high temperature sulfur removal from biomass-derived syngas–The impact of steam on capacity and sorption mode, Fuel 97 (2012) 612–620.

[53] X. Meng, W. de Jong, R. Pal, A.H.M. Verkooijen, In bed and downstream hot gas desulphurization during solid fuel gasification: a review, Fuel Process. Technol. 91 (2010) 964–981.